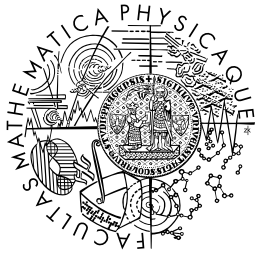

FACULTY
OF MATHEMATICS
AND PHYSICS
Charles University

BACHELOR THESIS

Lubomír Grund

Vortical motions in supergranules

Astronomical Institute of Charles University

Supervisor of the bachelor thesis:	doc. Mgr. Michal Švanda, Ph. D.
Study programme:	Physics
Study branch:	General Physics

Prague 2019

I declare that I carried out this bachelor thesis independently, and only with the cited sources, literature and other professional sources.

I understand that my work relates to the rights and obligations under the Act No. 121/2000 Sb., the Copyright Act, as amended, in particular the fact that the Charles University has the right to conclude a license agreement on the use of this work as a school work pursuant to Section 60 subsection 1 of the Copyright Act.

In ..... date ..... signature of the author

Title: Vortical motions in supergranules

Author: Lubomír Grund

Department: Astronomical Institute of Charles University

Supervisor: doc. Mgr. Michal Švanda, Ph. D., department

Abstract: In this thesis, we study vortical flows in solar supergranules in a specific dataset of velocity fields. In particular, the relation between heliographic latitude and vorticity near the respective centers of the supergranules is examined. There is a supported hypothesis that supergranular motions are influenced by Coriolis force, so we attempt to verify the hypothesis using aforementioned data.

Keywords: Sun, helioseismology, supergranulation, velocity fields

I would like to thank my supervisor doc. Michal Švanda for his patience and alacrity in his guidance for my thesis making effort. Furthermore, my thanks belong to everyone who persistently supported me during the creation of this thesis, in particular to my beloved mother.

Contents

Introduction

In this thesis, we study vortical flows in solar supergranules with a focus on the relation between heliographic latitude and vorticity near the respective centers of the supergranules. That relation is described by a supported hypothesis [1] that supergranular motions are influenced by Coriolis force. In addition to validation of our understanding of various solar phenomena, verification of this hypothesis is the goal of this thesis.

Our analysis is applied to a specific set of velocity maps and detected supergranule centers. The process of obtaining these is mostly beyond the scope of this thesis, however some aspects of used methods are discussed here in order to correct or at least explain/estimate inaccuracies in our results.

Solar Flow Patterns

Mass flows in the photosphere behave in nontrivial ways, with temporary patterns. There have been several explanations and attempts at description with various characteristic scales. The most widely known and accepted of those patterns are granules (with typical scales of 1.5 Mm [2] and lifetimes in orders of 10^3 seconds [3]) which are the results of solar convection.

Convection is a major mode of heat transfer in the so-called convective zone, which extends from near surface layers up to the depth of several hundred thousand kilometers [4]. Convection cell patterns are major cause for surface flow structures.

Another convection flow structure are supergranules with a typical horizontal scale of approximately 20–40 Mm[5], and a dynamical evolution time in orders of 1 day [5]. Supergranulation is our primary pattern of interest.

Data analysis

As implied earlier, the core of this thesis is performing analysis of externally acquired data. In particular, we are interested in vorticity near the centers of supergranules and its relation to heliographic latitude. According to the aforementioned hypothesis, these should correspond with the expected Coriolis force at given heliographic latitude.

Due to differential rotation of the Sun, the relation will not be trivial, with monotonous progression near the equator and possibly more complexity near the poles. Given the relative scarcity of similar works, comparison of our results with existing observations will be of limited significance.

1. Solar interior

The Sun is a star with radius slightly below $7 \cdot 10^8$m[6] and effective temperature $\approx$ 5780K[7]. The latter would make direct observations of regions bellow photosphere impractical in itself; the high opacity of subsurface regions of the Sun makes it almost impossible. Nonetheless there are indirect methods of studying the solar interior. Helioseismology offers an approach to making such measurements, which is further described in 2.1.

1.1 Structure of the Sun

There are several generally recognized layers of the Sun, distinguished primarily by the processes taking place there.

The core is the innermost layer. The bulk of fusion reactions take place in this region, therefore making it the heat source of the star (and by extension of the whole star system).

Further from the core lies the radiative zone characterized by the prevalence of transfer of the energy by radiative diffusion[1] and lack of fusion. It extends from the core to the tachocline – the border layer between the radiative and convective zone at the distance of roughly two thirds of solar radius.

For our purposes the more important is the convective zone. It occupies the region above the tachocline up until near the surface and is named after the convection phenomenon (and presence of convection cells, more deeply explored 1.2).

Photosphere is the "surface" layer of the sun that can be optically observed, meaning that the regions above are transparent for visible light while lower layers of the Sun are not. This has consequences for observation – to map the Sun below this layer indirect methods had to be developed, like helioseismology.

Regions above are considered Solar atmosphere, usually further divided into four regions: the chromosphere, the transition region, the corona and the heliosphere. They bear little influence on our problem.

1.2 Convection

Convection is a major mode of heat transfer in so called convective zone, which extends from near surface layers into the depth of (0.287 ± 0.003) solar radii [4].

Generally, convection can occur in fluid continuum when there is a temperature gradient in the direction of a gravitational force[2] (for ongoing convection there needs to be a heat source and sink in corresponding regions). The fluid in the lower potential gets heated, therefore its density decreases and buoyant forces are pushing the fluid to the higher potential. There it eventually cools down, its density increases and subsequently starts to "fall down" back to the heat source. This establishes circular vertical flow pattern, transporting heat from the source

[1] As opposed to convection typical for the next layer

[2] This is a necessary condition, but not a sufficient one

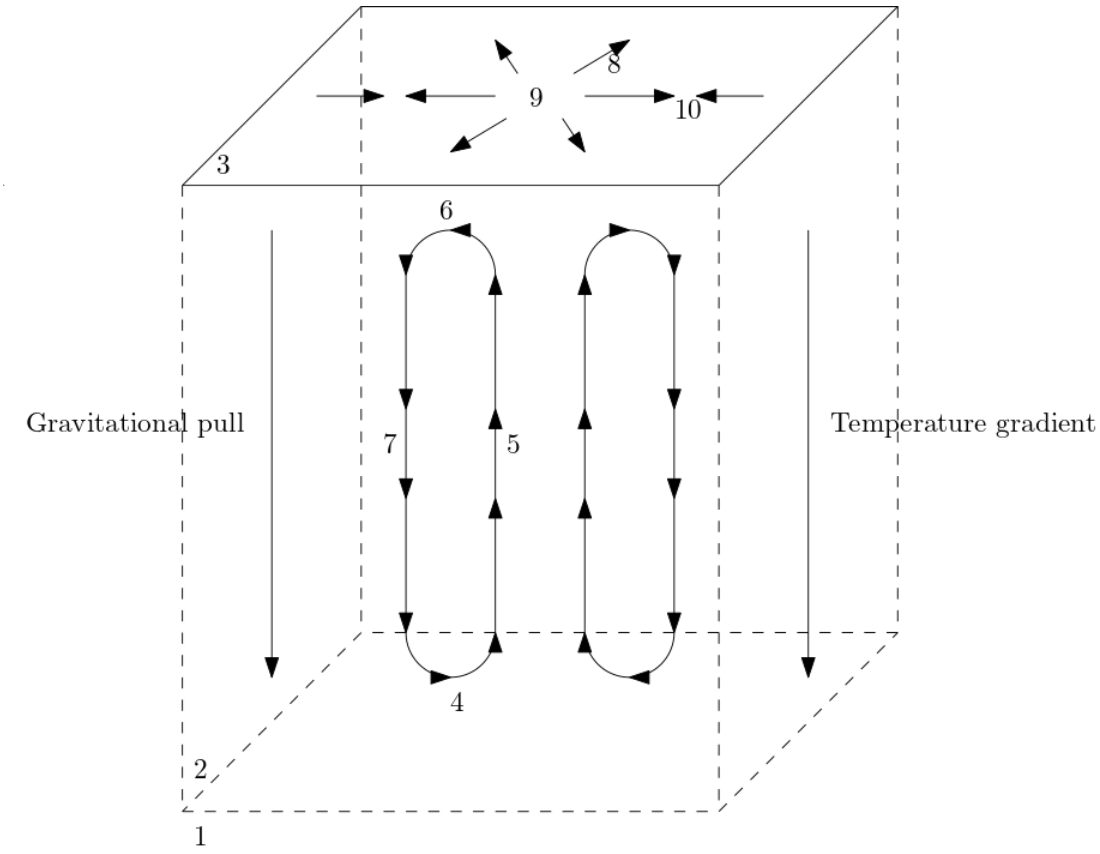

Figure 1.1: Schematic simplification of solar convection flows: 1 radiation zone, 2 convection zone, 3 photosphere, 4 matter gets heated, 5 hotter (and therefore less dense) matter flows upward, 6 difluence of upward stream, 7 colder matter flows downwards, 8 convection flow patterns visible on the "surface", 9 outflow region, 10 inflow region

to the heat sink in the upper layers. These motions are ilustrated by the Figure 1.1.

In stellar physics, the condition for convection to occur is referred to as the Schwarzschild criterion [8]. Specifically, it implies instability such that if an element is displaced upwards, it keeps rising. Assuming an adiabatically expanding element of ideal gas, the criterion takes the form of:

$$\frac{\mathrm{d}\log T}{\mathrm{d}\log p} < 1 - \frac{1}{\gamma}, \tag{1.1}$$

where T is temperature, p is pressure and γ is Poisson constant of the element.

Convection cell patterns are major cause for surface flow structures. Those structures facilitate the transfer of matter from convective upstreams to downstreams – meaning the surface velocity patterns conform to those of convective cells.

1.3 Differential Rotation

The Sun is subject to rotation, however it does not rotate as a rigid body but even the average rotation rate differs for specific latitudes (and depths). This is called

differential rotation. In [9] it is shown, that for various measuring techniques the apparent rotation profile can be approximated as

$$\omega = A + B \sin^2 \varphi + C \sin^4 \varphi \tag{1.2}$$

where ω is rotation rate, φ is heliographic latitude and the coefficients vary for specific techniques, however for sidereal rotation their value is roughly $A \approx 2.97 \cdot 10^{-6}$ rad s^{-1}, $B \approx -0.48 \cdot 10^{-6}$ rad s^{-1} and $C \approx -0.36 \cdot 10^{-6}$ rad s^{-1}[9].

More specifically, using helioseismological methods rotational depth profile has been observed, with nontrivial progression throughout convective zone with particularly steep gradients in near-surface layers, as in [10].

2. Methodology

2.1 Helioseismology

Time-distance helioseismology[11] is a method of studying the solar interior (including flows). It utilizes knowledge about various solar oscillations modes and dependence of their dispersion relations on different parameters of the medium. By cross-correlating disturbances in concentric annuli we can calculate travel times propagating waves and use previously mentioned knowledge to formulate the inverse problem – to infer values of parameters in subsurface layers, more specifically flow vector fields.

Solving aforementioned inverse problems is a nontrivial task. —The popular approach is using semi-empirical numerical methods, validated by comparison with otherwise obtained data or simulation outputs.

2.2 Our datasets

As a datasource for our analysis effort we will use a series of enhanced velocity maps of solar matter flows. Each map consists of multiple scalar fields (3 components of velocity and center-detection mask) represented on a spatial 512×512 matrix. Each matrix element corresponds to a point in azimuthal equidistant projection (sometimes referred to as the Postel projection) concentric with the current map. In said center, distance between neighboring elements (in a row or column) is approximately 1.3920 Mm or $2 \cdot 10^{-3} R_{\odot}$.

For our purposes, shifts in heliographic longitudes between maps are irrelevant, so the only distinguishing feature of a map as a whole is the heliographic latitude of the center of projection. Amongst our maps, only three different center latitudes are present: 35° heliographic southern latitude with 1108 maps, heliographic equator with 1108 maps and 35° northern latitude present in only 1106 maps.

The aforementioned "center-detection mask" is simply a matrix with elements of value 1 for the supposed center of a supergranule and 0 everywhere else.

2.2.1 Origin of the data

Flow maps in our datasets were obtained by utilising time-distance helioseismological methods on raw data from *Solar Dynamics Observatory* (SDO), *Helioseismic and Magnetic Imager* (HMI)[12, 13]. Specificcaly, the SOLA[14] inversion method has been used on f-mode oscillations (surface gravitational waves, sometimes called fundamental modes).

The centers of the supergranules have been detected using a watershed algorithm with respect to divergence, which is described in [15].

2.3 Data analysis

Vorticity $\boldsymbol{\mu}$ usually defined as

$$\boldsymbol{\mu} = \nabla \times \boldsymbol{v}, \tag{2.1}$$

where $\boldsymbol{v}$ is velocity field, describes local "swirliness" of a continuum. For our aplications, we are only interested in motions in a near surface manifold of volume occupied by the Sun, therefore a scalar field μ – corresponding with the normal component of general vorticity $\boldsymbol{\mu}$ – will suffice. μ can be expressed as

$$\mu = \frac{\partial v_y}{\partial x} - \frac{\partial v_x}{\partial y}, \tag{2.2}$$

where x and y are local cartesian coordinates and v_q are q-components of velocity field.

For calculation of field derivatives we utilised the:

$$\mathcal{F}\Big[\frac{\mathrm{d}}{\mathrm{d}x_i} f(\boldsymbol{x})\Big](\boldsymbol{\xi}) = 2\pi i \xi_i \mathcal{F}\Big[f(\boldsymbol{x})\Big](\boldsymbol{\xi}), \tag{2.3}$$

property of Fourier transform where $\mathcal{F}$ denotes Fourier transform and x_i, ξ_i denotes $i-$th component of argument of f, resp. of its Fourier image. For the vorticity map we then get

$$\mu(x,y) = 2\pi i \mathcal{F}^{-1}\Big\{(-\xi_y \mathcal{F}\Big[v_x(x,y)\Big] + \xi_x \mathcal{F}\Big[v_y(x,y)\Big]\Big\}, \tag{2.4}$$

where x and y are spatial coordinates, ξ_x and ξ_y their frequency domain equivalents, v_x and v_y are coresponding components of velocity $\boldsymbol{v}$ and $\mathcal{F}^{-1}$ denotes inverse Fourier transform.

Specifically, `fft2` (2-D fast Fourier transform) Matlab$^{\mathrm{TM}}$ implementation was used.

2.3.1 Coordinates transformations

As stated earlier, our datasets are given in azimuthal equidistant projection and corresponding coordinate system. Its relation to spherical coordinates are given in [16]. Since the oblateness of the Sun is well bellow 0.1% [17], we will consider only formulas for spherical surface:

$$X = \Big(\frac{a}{\sin a}\Big) \cos\varphi_0 \sin(\lambda - \lambda_0), \tag{2.5}$$

$$Y = \Big(\frac{a}{\sin a}\Big)\Big[\cos\varphi_0 \sin\varphi - \sin\varphi_0 \cos\varphi \cos(\lambda - \lambda_0)\Big], \tag{2.6}$$

where X and Y are Postelian coordinates; φ and λ are corresponding heliographic latitude and longitude; φ_0 and λ_0 are heliographic latitude and longitude of the central point of projection and for parameter a:

$$\cos a = \sin\varphi_0 \sin\varphi + \cos\varphi_0 \cos\varphi \cos(\lambda - \lambda_0). \tag{2.7}$$

We need to investigate behavior for $\sin a = 0$. Since

$$a = \sqrt{X^2 + Y^2} \tag{2.8}$$

holds, only two points[1] could be problematic: the central point of projection (φ_0, λ_0), where $X = Y = a = 0$ and the antipode of the central point where $a = \pi$, which does not have point Postelian image anyway. Since at the central point the values of coordinates equal their limits, the (2.5) and (2.6) are differentiable on the inside all Postelian maps.

Furthermore, for the inverse relation we get

$$\varphi = \arcsin\left[\cos a \sin\varphi_0 + \left(Y \sin\varphi_0 \frac{\sin a}{a}\right)\right], \tag{2.9}$$

$$\lambda = \begin{cases} \lambda_0 + \arctan\left[X/(a\cos\varphi_0 \cot a - Y \sin\varphi_0)\right] & \text{for } |\varphi_0| \neq \pi/2, \\ \lambda_0 + \arctan(-\frac{X}{Y}) & \text{for } \varphi_0 = \pi/2, \\ \lambda_0 + \arctan(\frac{X}{Y}) & \text{for } \varphi_0 = -\pi/2. \end{cases} \tag{2.10}$$

2.3.2 Statistical processing

In an effort to visualize observed dependency of supergranular vorticity on heliographic latitude (like in section 3.3), we cluster individual supergranules into "bins" by their latitude. Such bins contain large number of individual datapoints and we are interested primarily in four attributes of a bin: average latitude $\bar{\varphi}$ of detected supergranules in a bin, average vorticity $\bar{\mu}$, and standard deviations (σ_φ and σ_μ) of those quantities.

[1] since distances from the center of the projection are invariant [16]

3. Results

3.1 Initial results

As described in 2.3.2, in order to visualize the relation between vorticity near the centers of the supergranules and heliographic latitude we divide calculated data-points into bins (by their latitude) with certain width and plot average vorticities for each bin. The result can be seen in Figure 3.1.

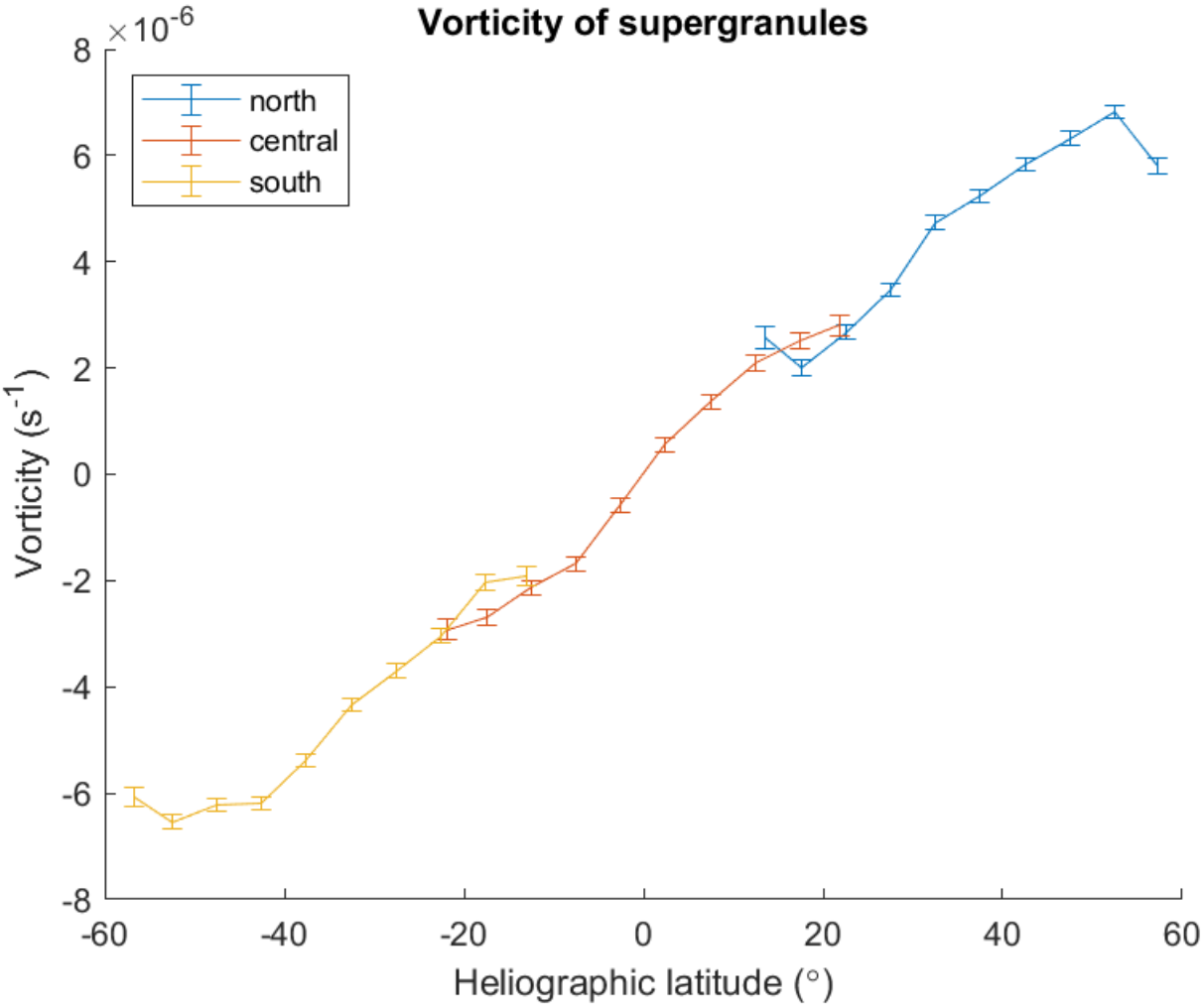

Figure 3.1: Dependence of supergranular vorticity on heliographic latitude before applying corrections – bin size 5°

Qualitatively speaking, this result roughly agrees with the expected outcome (assuming this vorticity is result of Coriolis force) with the exception of marginal bins. Ignoring those, there is clear discontinuity between data from different regions. This discrepancy needs to be explained in order to obtain any significant and conclusive outputs from this thesis.

3.2 Corrections

In light of the inconsistency of initial results and several observations about the original datasets, there are several alterations to our process that need to be implemented.

3.2.1 Projection distortion

Like every projection of sphere onto a plane, Postel projection distorts our spherical reality. Figure 3.2 is a visualization of the relation between Postelian and heliographic coordinate systems in the region of our datasets. It is clear that heliographic coordinates might significantly disagree with their linearly approximated estimates from the Postelian system (especially in the northern and southern regions). It shows that we need to calculate the actual heliographic latitudes of our supergranules for the purposes of our analysis.

One should not be distraught by the ominous appearance of the northern region in Figure 3.2. Keep in mind that that from the equator and on the scales used the projection onto the heliographic coordinate grid itself bears significant distortion. To gain a better idea about local distortions, see Figure 3.3. It is evident that local distortion is not as severe as Figure 3.2 would suggest.

To correct the distortion, when constructing bins for 3.3 their heliographic coordinates are considered instead of the Postelian ones. The need for further corrections is discussed in 4.2.1.

3.2.2 Average bin latitude

As one can see in Figure 3.4, distribution of detected supergranule centers is not uniform within our maps. Detected centers reside only in a circular area with a disproportionate amount on its circumference. One of the consequences of this is uneven distribution of centers within a bin. This can be partially corrected by calculating the average position of supergranule centers within a bin instead of using the center of a bin itself. Supergranule detection bias can have further repercussions which are discussed in 4.2.3;

3.2.3 Cropping

In Figure 3.5, one can observe that areas up to 100 Mm from the borders in every map are subject to error. As a remedy, we can ignore supergranules near the borders, which however could significantly lower the amount of datapoints in certain bins (see Figure 3.4). Since the anomalies tend to be bounded by the parallels of the margins, we will crop a fixed number of pixels (instead of using conditions with physical relevance). The nature of the restriction of these anomalies suggests that this can be the result of convolution with aforementioned kernel, where maps are processed with periodic condition.

3.3 Final results

The results after the application of all corrections from 3.2 are plotted in Figure 3.6. It is clear, that the inconsistency between regions remain significant, however the results are qualitatively consistent with our expectations. Further significance of our results is discussed in 4.

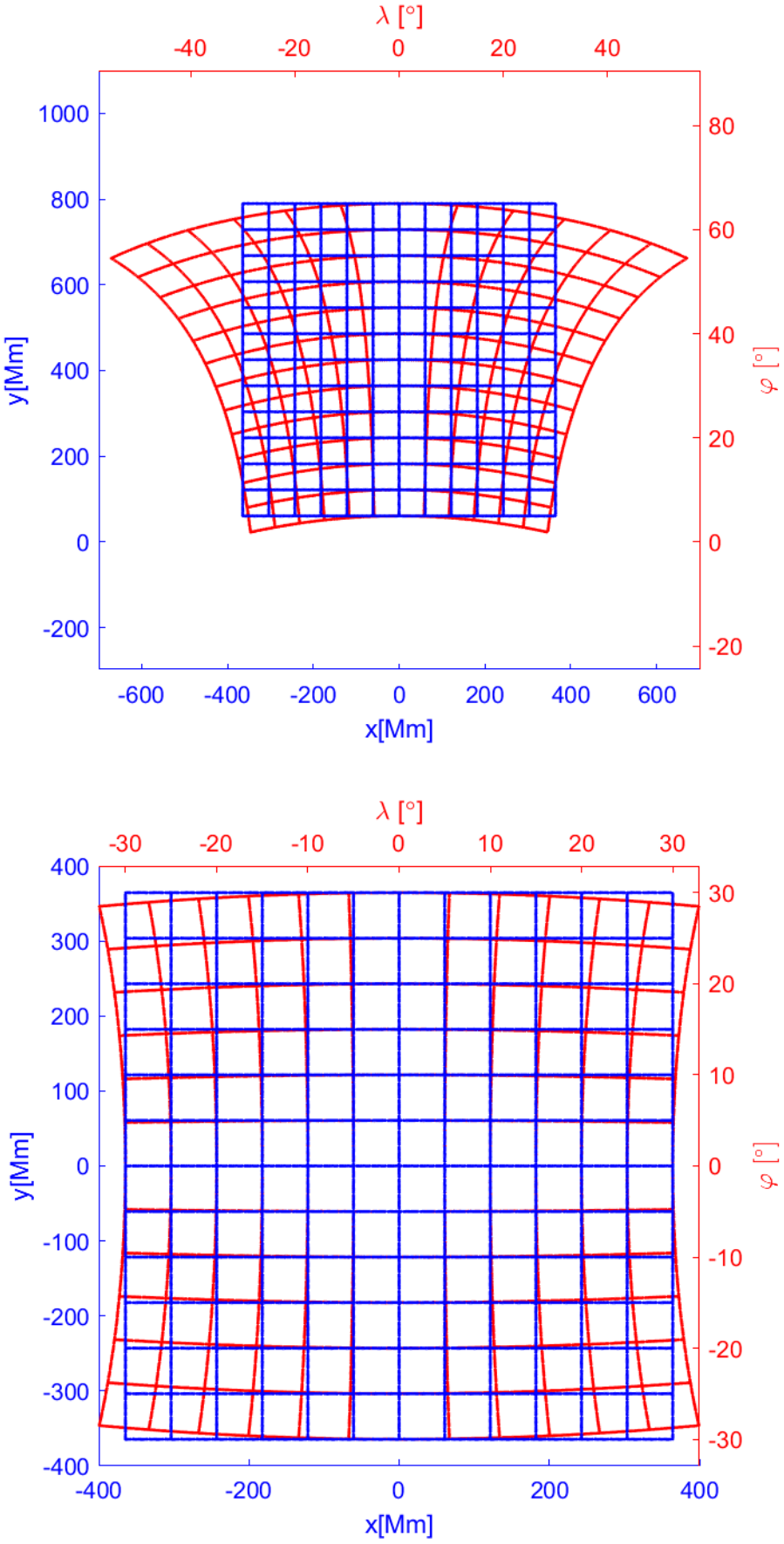

Figure 3.2: Blue: Postel coordinate grid with parameter equivalent of 5°. Red: the same grid plotted in heliographic coordinates. Top: north region. Bottom: central region.

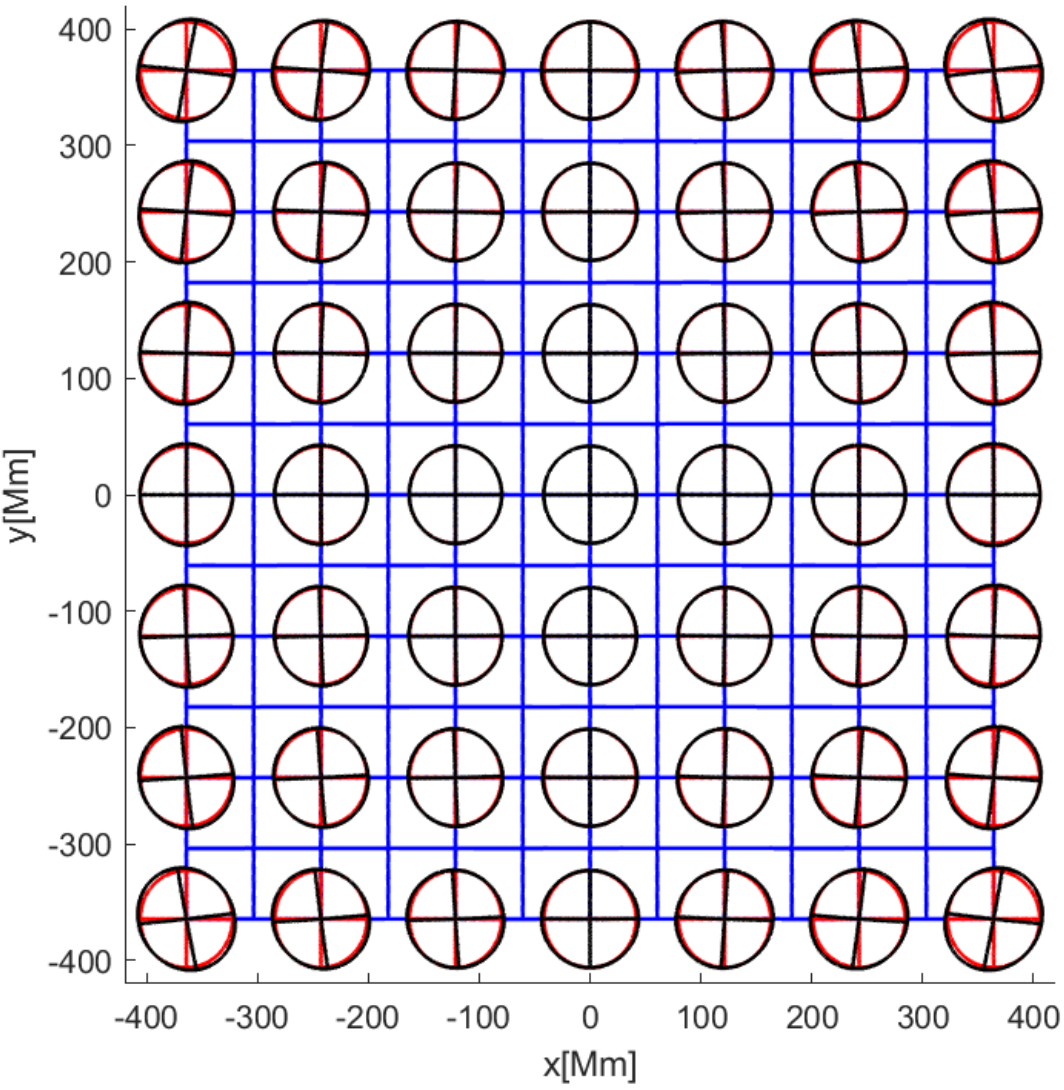

Figure 3.3: Blue: Postel coordinate grid with parameter equivalent of 5°. Black: Cirles with radius approx. 42 Mm, centres in grid vertices and radii in cardinal directions. Red: Analogue of blue, but in Postelian basis.

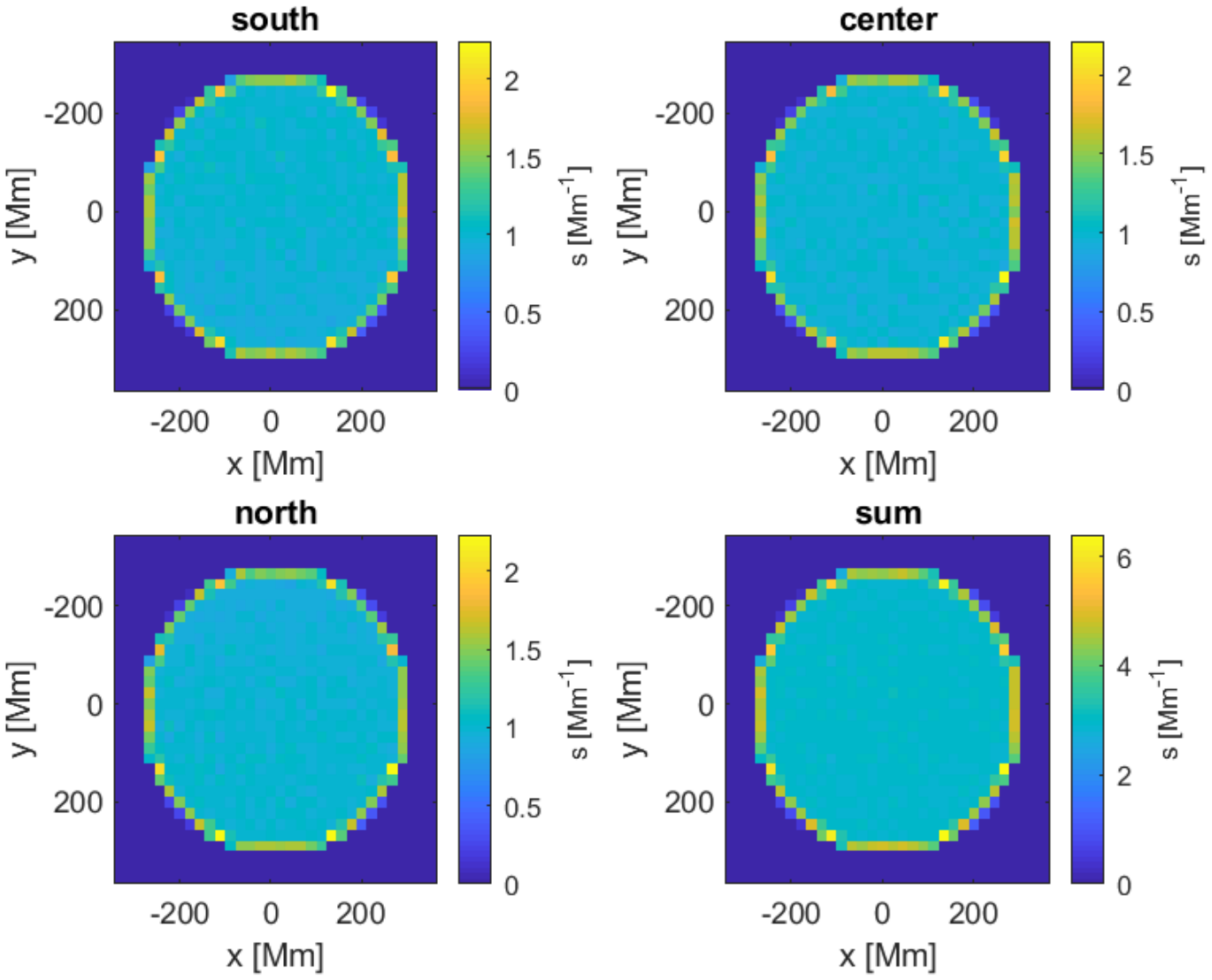

Figure 3.4: Density s of detected centers for all regions and their total.

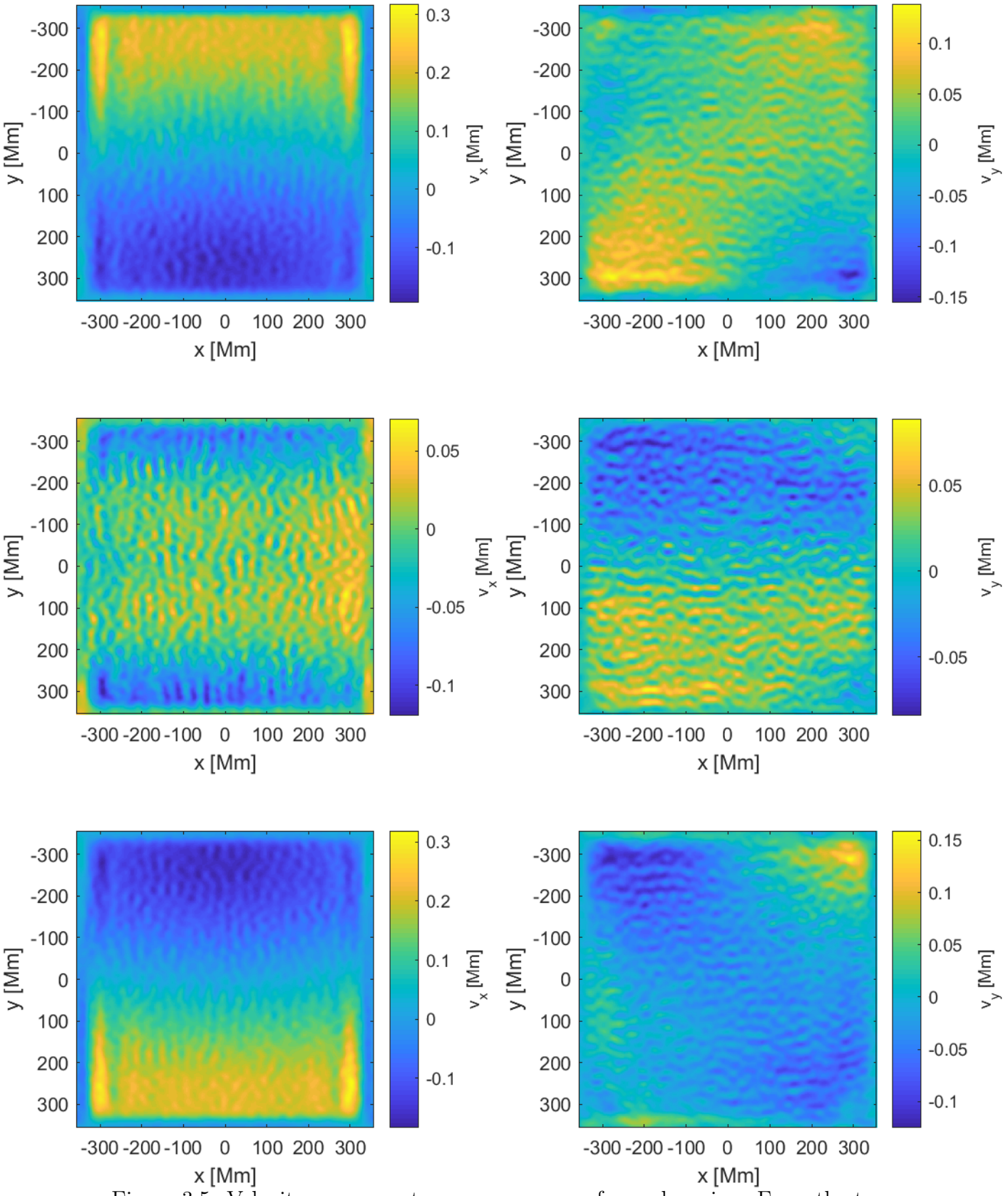

Figure 3.5: Velocity components on average map for each region. From the top: northern, central and southern region.

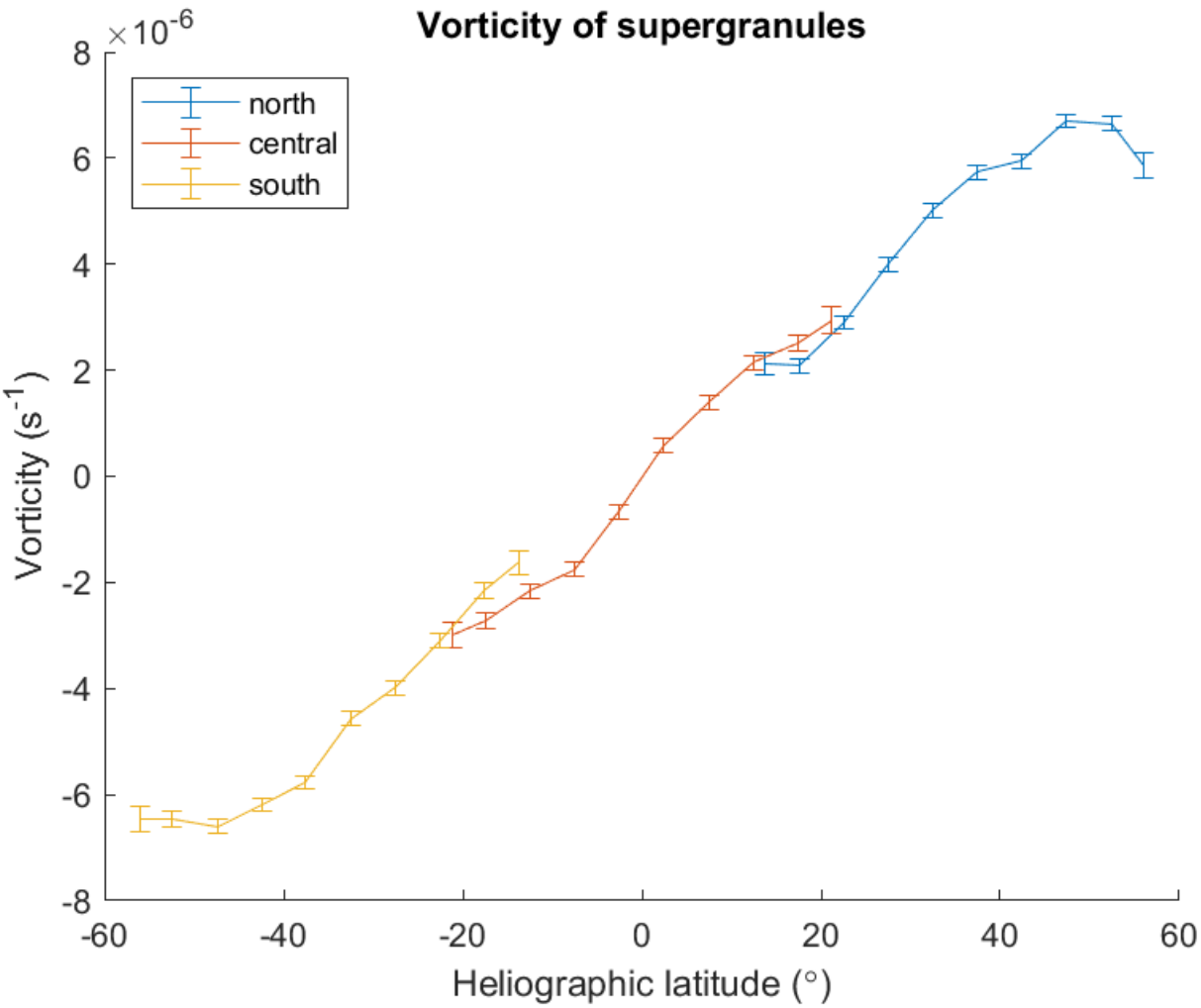

Figure 3.6: Dependence of supergranular vorticity on heliographic latitude with bin size of 5° and marginal 60 px cropped.

4. Discussion of the results

In this section we attempt to interpret our results. Specifically, we discuss the weaknesses of our methodology both by further analysing used methods and looking at some aspects of our datasets at different stages of processing. Furthermore, we estimate influence on our results from various potential sources of inaccuracies and finally compare our results with already published results and with a hypothesis about the origin of investigated phenomenon.

4.1 Average Supergranule

To gain a better understanding about our dataset's nature and weaknesses, we will first observe results of our methods on average velocity fields around supergranule centers. By "*average velocity fields around supergranule centers*" we mean that for every supergranule center in every field we take a 201×201 pixel cropped velocity field, shift it so that the supergranule center would preside in the center pixel and then compute an average field from those (this will be independently for the projection latitude centers (southern, central, northern)).

The amount of detected supergranule centers in southern, central and northern fields were total of 293 056, 289 551 and 291 099 respectively.

4.1.1 Total horizontal velocity

Here, one would expect radially symmetrical results, with nontrivial values around the center up to the distance of characteristic supergranular sizes. Beyond that, the fields would ideally average to values near zero (or background differential rotation average). The only major differences between different heliographic latitudes should be the results of the aforementioned differential rotation.

The results roughly match our expectations. In the (more detailed) right column of Figure 4.1, it is clear that on the supergranule-dominant scales results are fairly similar. On the other hand, in the left column there is a background present with symmetries and gradients explainable by differential rotation of the solar matter. However a closer look shows some noise with roughly octagonal symmetry (better visible in Figure 4.2). Due to its symmetry, it is possible this is a result of convolution with imperfect kernel 4.2.4 which also has this symmetry.

4.1.2 Radial and circular horizontal velocity

For radial velocity, both expectations and results are fairly similar to 4.1.1 with the difference that it can be described and explained in more detail. For example in Figure 4.4 multiple zones with radial symmetry can be recognized. Coming from the center:

1. Center – radial velocity cannot be calculated for central pixel, so it is dark.

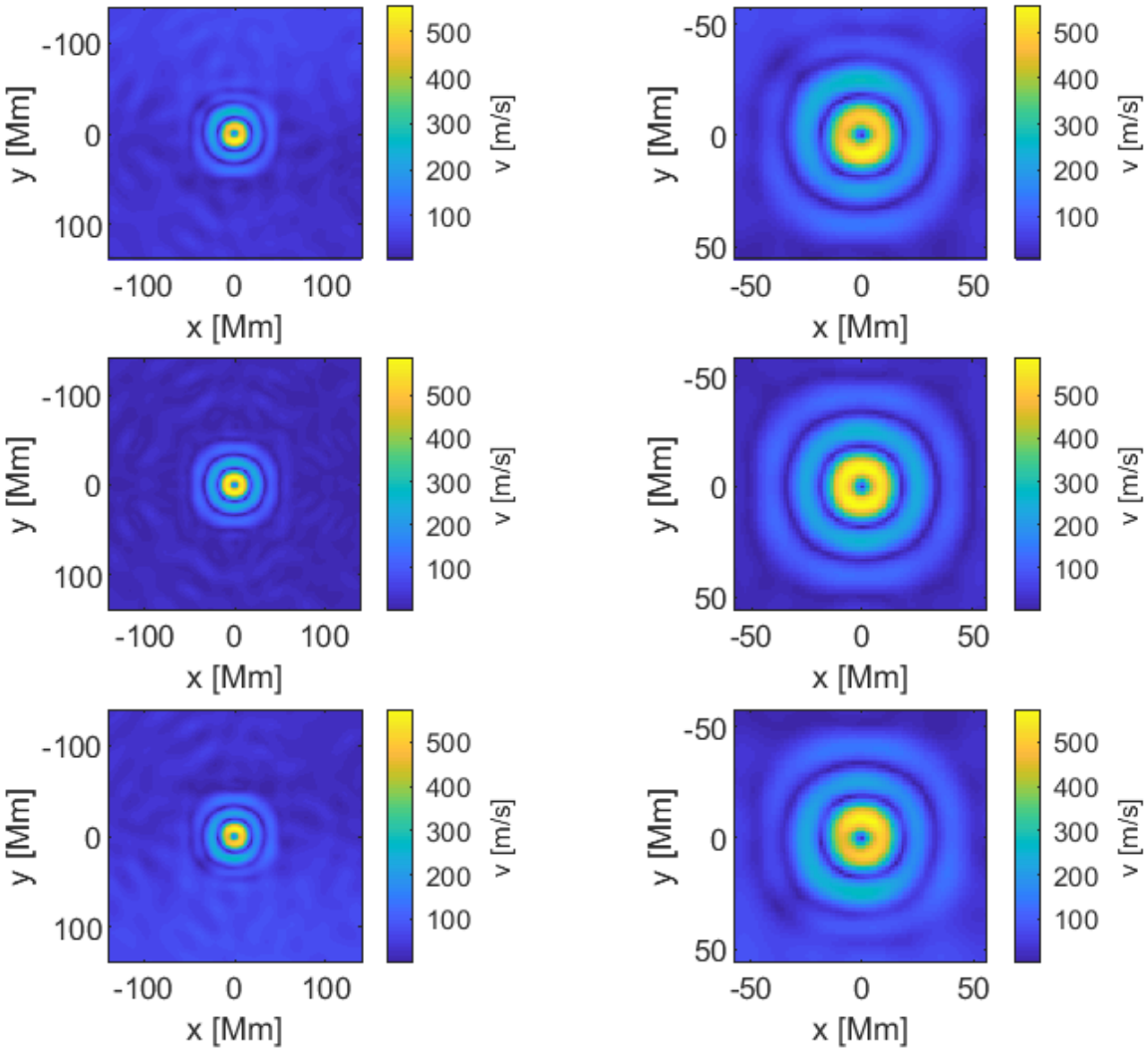

Figure 4.1: Horizontal velocity component in the vicinity of average supergranule. Rows correspond with (from top to bottom) northern, central, southern.

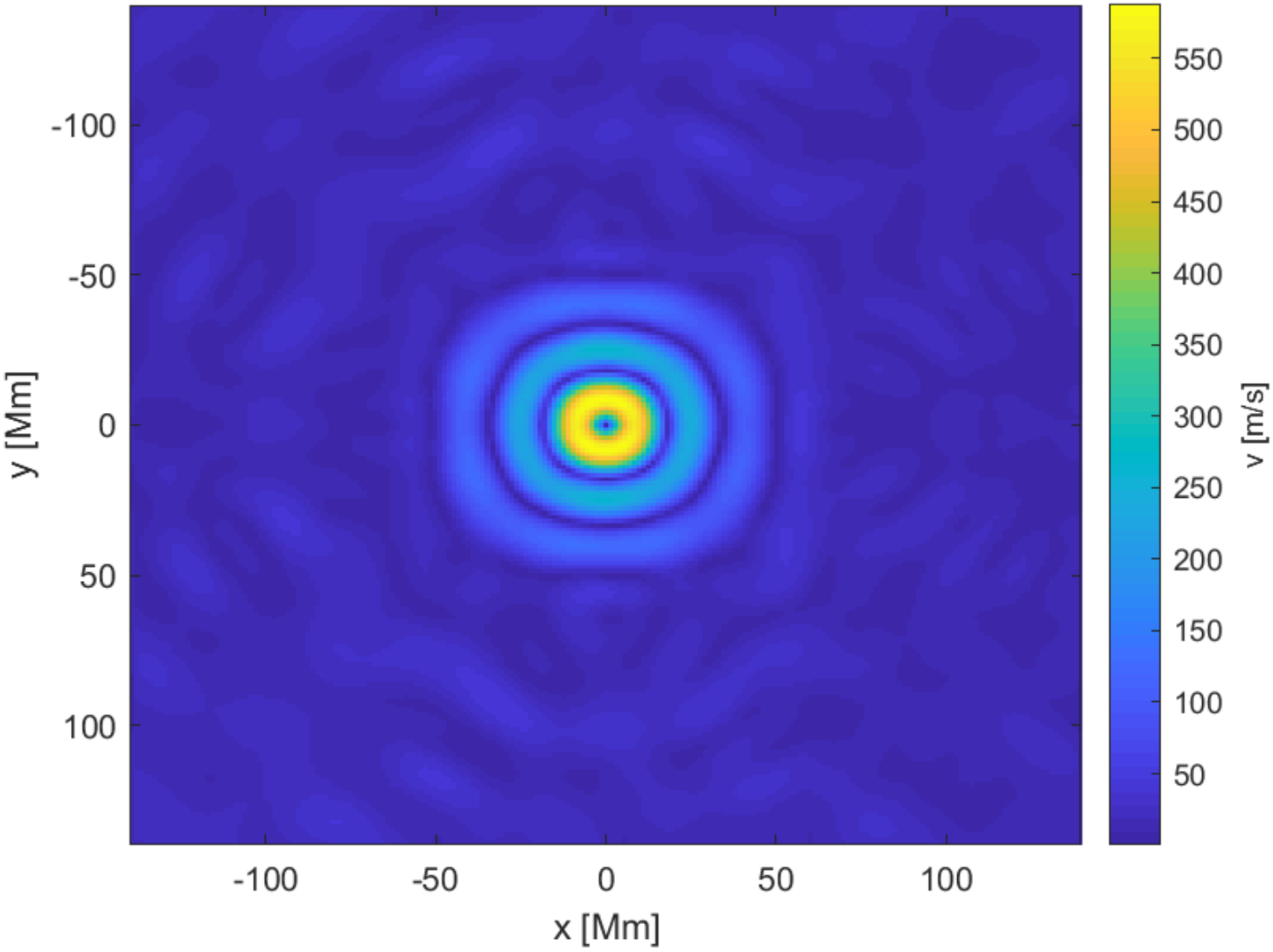

Figure 4.2: Horizontal velocity component in the vicinity of average supergranule for the central region

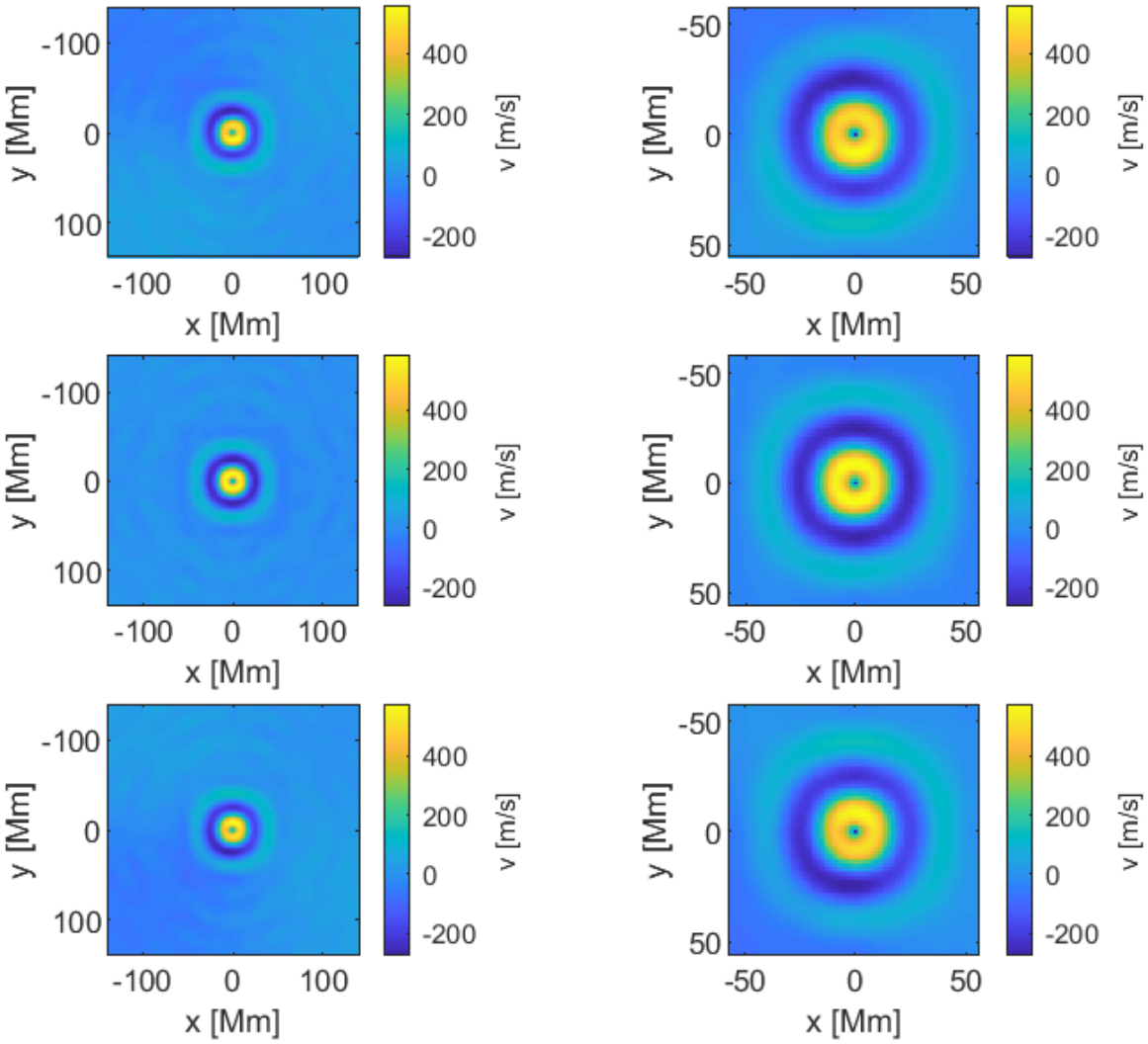

Figure 4.3: Radial velocity component in the vicinity of average supergranule. Rows correspond with (from top to bottom) northern, central, southern.

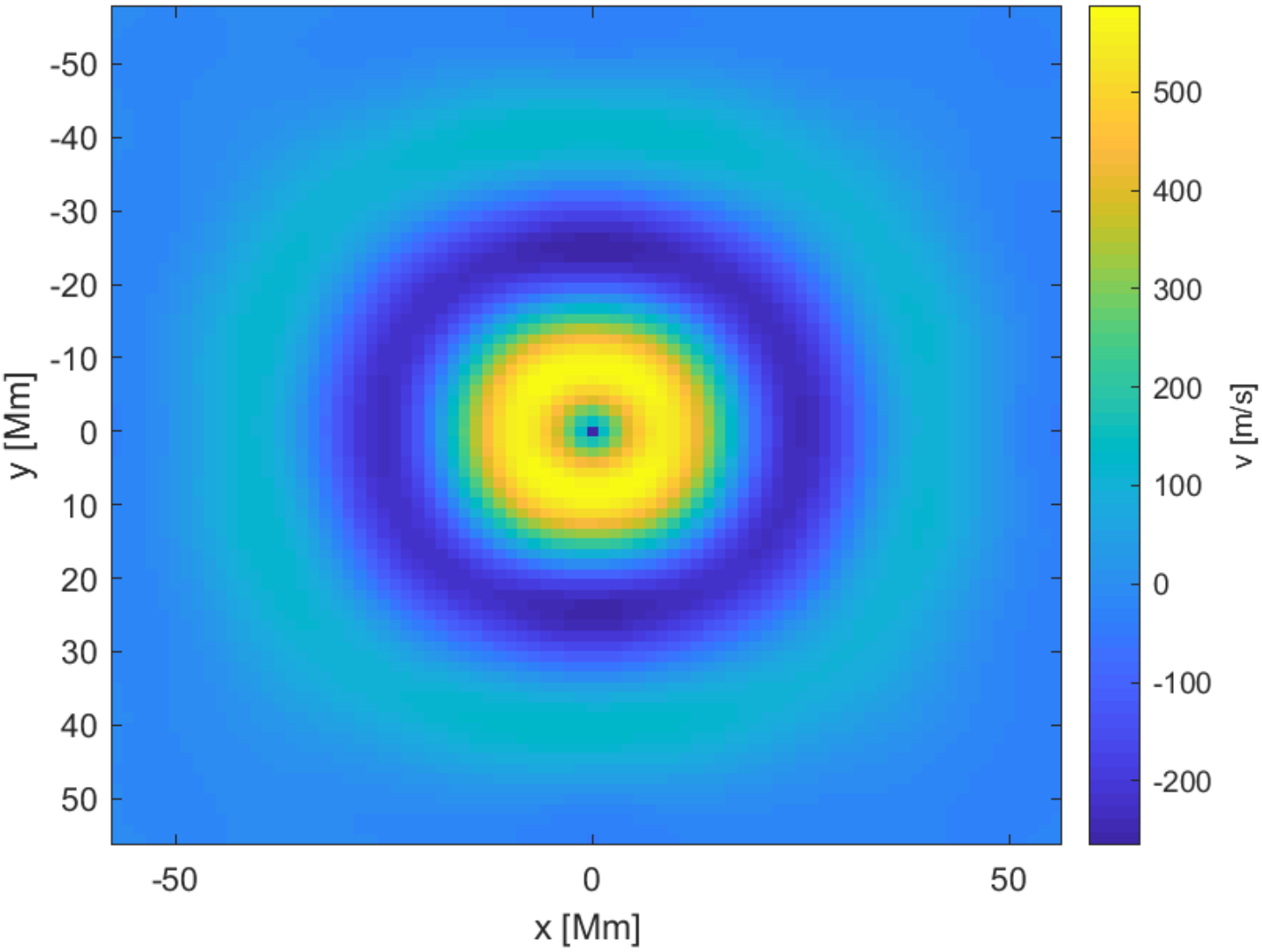

Figure 4.4: Radial velocity component in the vicinity of average supergranule for the central region

2. Supergranule – radial flow raises because of both outflow region near the center of the supergranule and inflow regions further out. Can be compared with Figure 4.6

3. Neighbouring supergranulae – once past average distance to the inflow region, the sign of radial flow changes – on matter flows towards the center

4. Beyond distance to the average neighbouring supergranule center, radial flow reverts back to the outward direction.

5. Points 3) and 4) can periodically continue with decreasing intensity – referring to the "neighbours of higher degree", or pair distribution function.

Figure 4.5 displays circular horizontal velocity component with regards to the supergranule center. Velocities are about an order of magnitude lower than Figure 4.4, however their peculiar symmetrical nature suggests they do not have natural origins. Its likely cause is either imperfect convolution kernel or distortions caused by projection distortions (see 4.2.1). Its relatively high values relative to radial components also speaks to the low reliability of our results in general.

4.1.3 Horizontal divergence and rotation

The divergence around the average supergranule is visualized in Figure 4.6. Its explanation is analogous to the explanation of the radial component map in 4.1.2 but with different qualitative relations to specific regions – positive values in the outflow regions, negative in the inflow regions, near zero in between.

Figure 4.7 shows rot_z (vorticity). The takeaway from the graph is similar to 4.5 – relatively strong systematic artifacts with similar symmetry.

4.2 Possible sources of inaccuracies

In 3.2 we described the implementation of several corrections to improve our results. In this section we will discuss possible sources of additional inaccuracies whose corrections are beyond the scope of this thesis.

4.2.1 Projection distortions

In 3.2.1 we describe the need to calculate the physical coordinates of the centers of supergranules. That correction has been implemented, however distortion of the flow vectors themselves is not taken into account and neither is transformation of differential operators. Both of these are sensitive to local distortion which is visualized in Figure 3.3. Considering the cropping correction described in 3.2.3 and detected center distribution visualised in Figure 3.4 one can see that only the innermost nine circles are inside the relevant region. Relevant circles show only

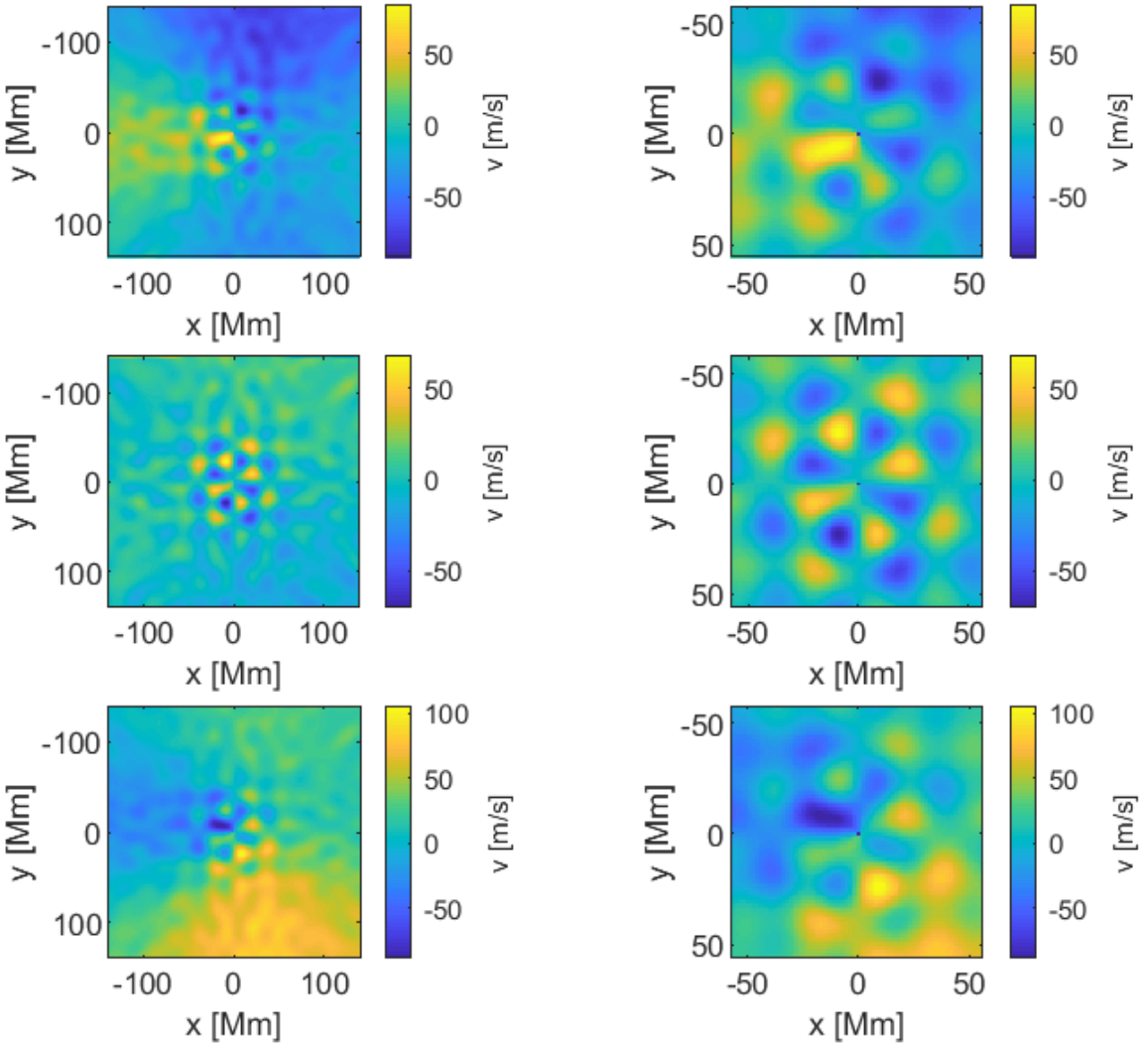

Figure 4.5: Circular velocity component in the vicinity of average supergranule. Rows correspond with (from top to bottom) northern, central, southern. Right column contains zoomed in version of the left column.

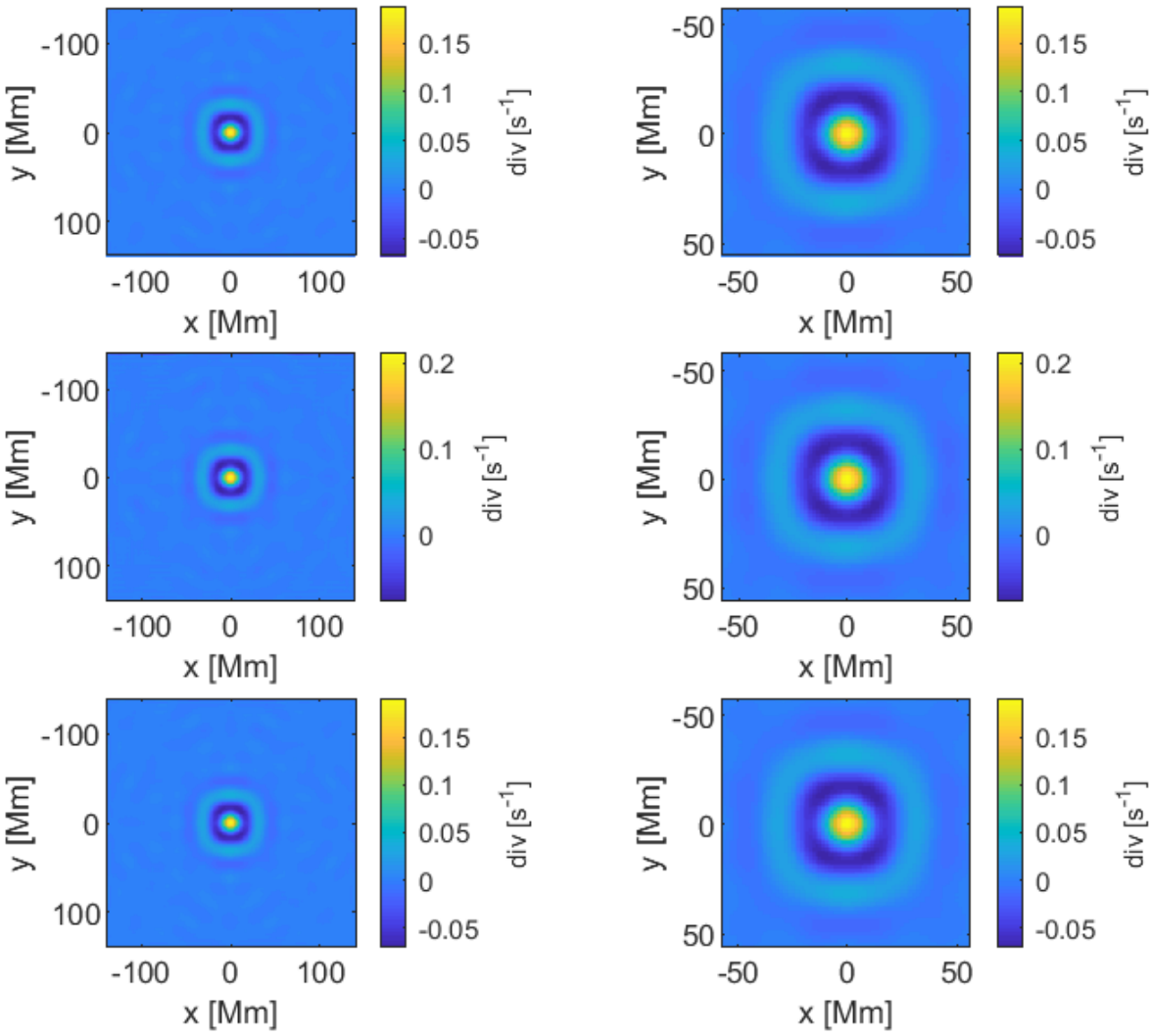

Figure 4.6: Divergence of horizontal velocity in the vicinity of average supergranule. Rows correspond with (from top to bottom) northern, central, southern. Right column contains zoomed in version of the left column.

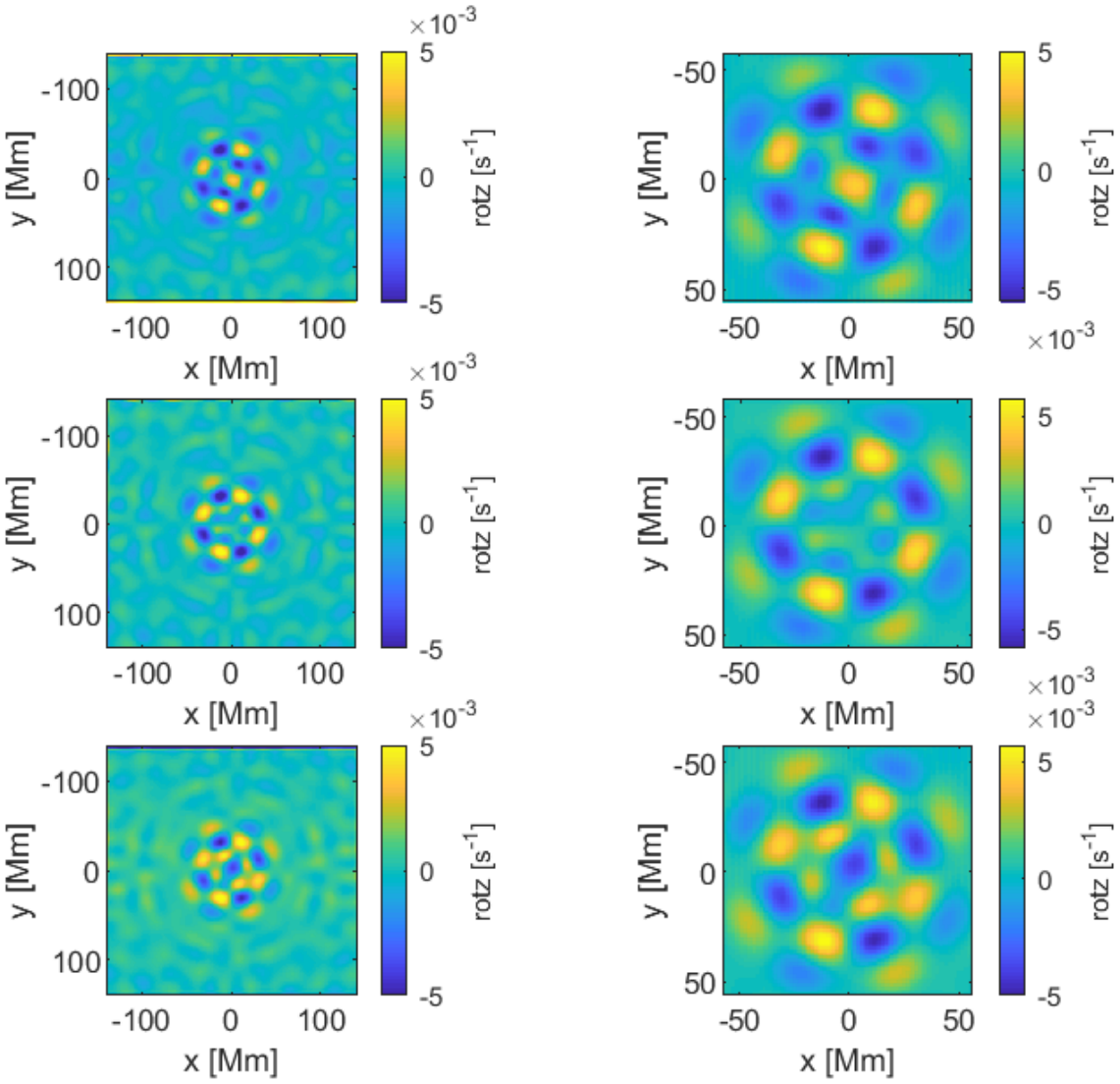

Figure 4.7: Vorticity in the vicinity of average supergranule. Rows correspond with (from top to bottom) northern, central, southern. Right column contains zoomed in version of the left column.

miniscule deviations, therefore we can assume that systematic error produced by this is also small.

To precisely calculate the contribution of this effect (or corrected values) the Jacobian matrix field of the transformation would need to be calculated.

4.2.2 Differential rotation

Due to the presence of persistent flows – differential rotation, our calculated vorticity might include undesirable components. However, our initial velocity maps should have already been compensated for differential rotation[1]. The rotational profile subtracted is similar to (1.2) but with respect to Postelian coordinates instead of heliographic and with different coefficients[2].

Due to projection distortions it is still possible that differential rotation causes systematic bias among our data. This effect should be independent of the presence of a supergranule or its outflow region, therefore by examining average vorticity maps for each region we can estimate the influence of this effect. Such maps are displayed in Figure 4.8. There is a clear latitude-dependence character along with a lot of noise. The same map is displayed differently in Figure 4.12 and Figure 4.13.

In Figure 4.9 there is the outcome of the application of the "bin" procedure from 3.3 on average vorticity maps. In comparison with Figure 3.6, it appears that discrepancies in Figure 4.9 could account for a major part of the discontinuity in the final results. Due to the high noise and extreme supergranule center density in particular areas, it is problematic to apply a correction based on this observation. Either much more data is needed or implementation of a nontrivial smoothing function for the background vorticity would be required.

4.2.3 Supergranule detection bias

As mentioned in 3.2.2, supergranule center detection bias can have consequences beyond shifting the average latitude of certain bins. Since the reason for this particular center distribution is not known, it is impossible to fully estimate the potential influence of underlying bias.

A possible reason for this distribution is regional restriction for watershed algorithm centers – a supergranular cell with its center outside said region is assigned divergence extreme inside the region. This would likely result in the regresion of vorticity for supergranules in affected regions toward background values. Since every bin has a different ratio of perimeter supergranules, each can be affected differently. After cropping in 3.2.3 marginal bins in every region are not affected, so this cannot be an explanation for discontinuity between regions.

Independently of the validity of detection, we can discuss how this specific distribution can affect our results. In this regard, it can exacerbate effects from 4.2.1 or other distortions from measuring travel times or inversion method (SOLA).

[1] `http://www2.mps.mpg.de/projects/seismo/Track%27n%27Map/TracknMap.html`, May 13th, 2019

[2] see [1]

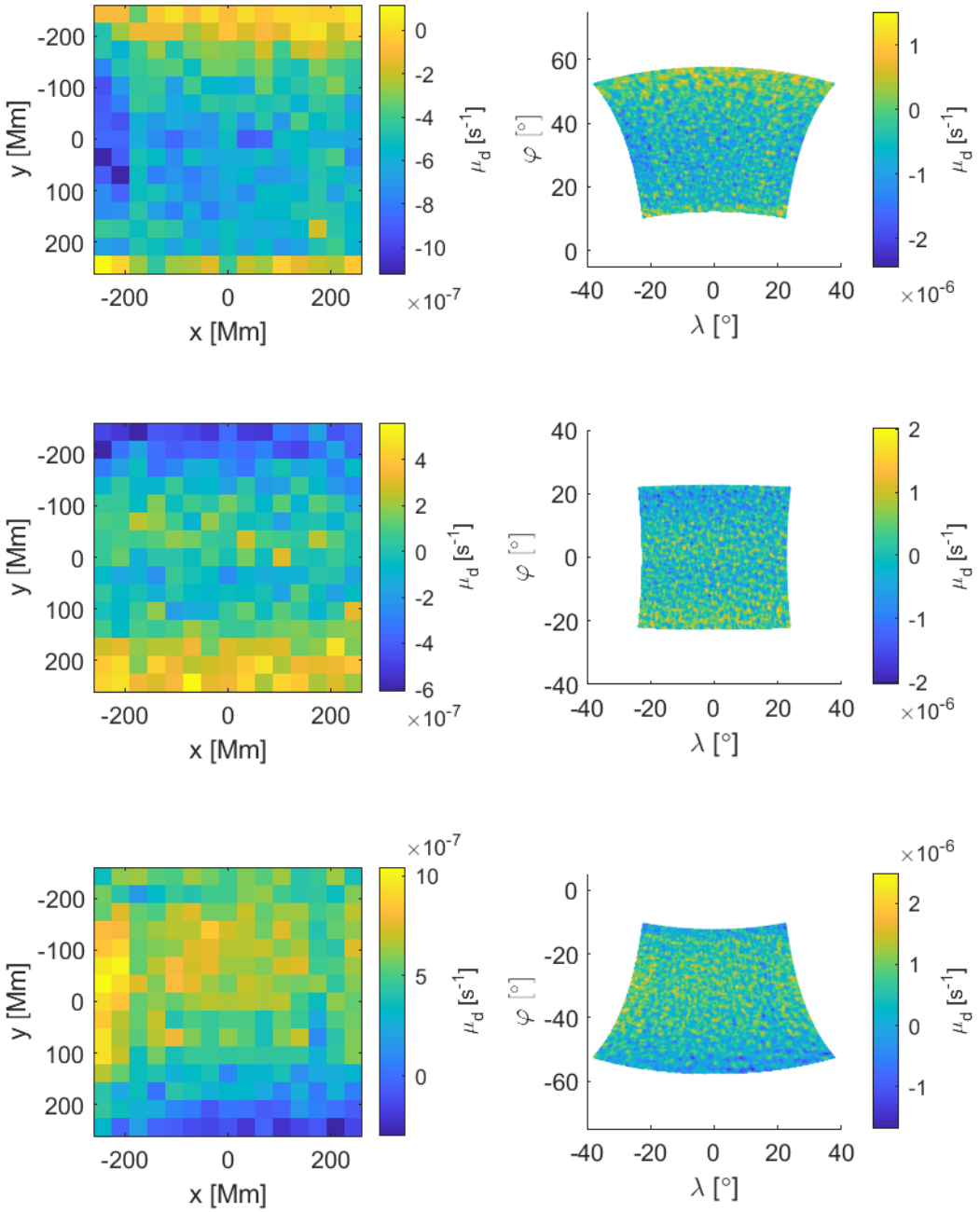

Figure 4.8: Average vorticity μ_d (regardless of supergranules). Rows from top: north region, central region, south region. Left column: average value of μ_d for square tiles in Postelian coordinate system, right column: average μ_d map in heliographic coordinates.

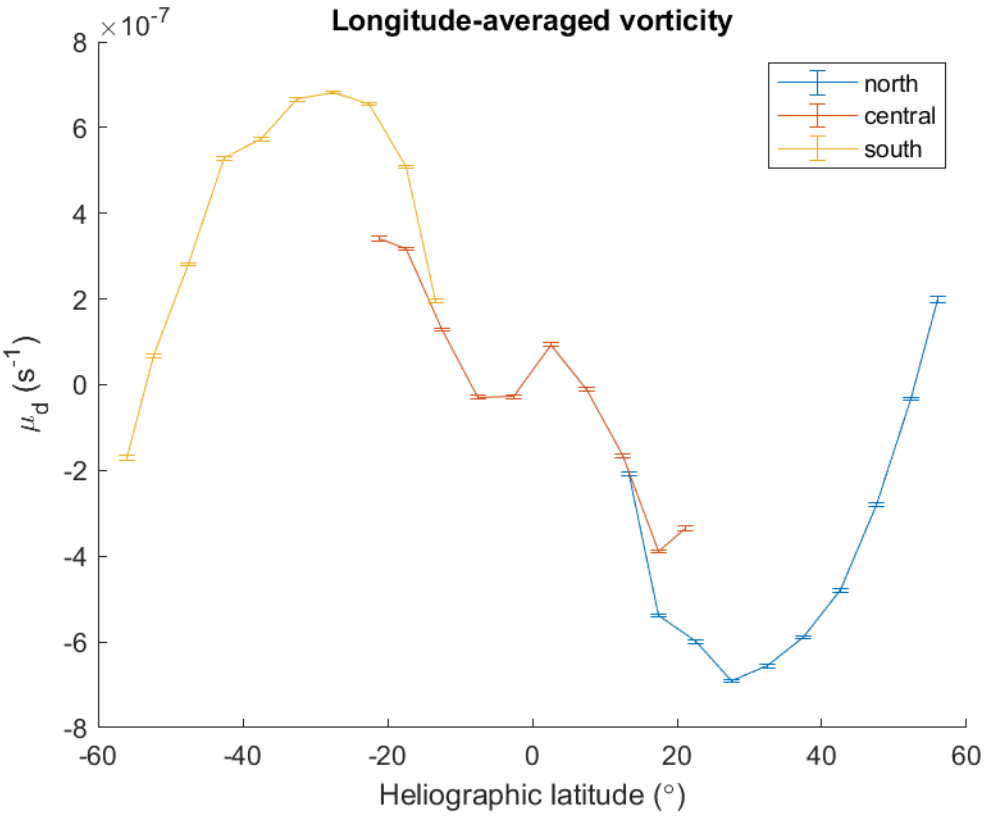

Figure 4.9: Average vorticity μ_d (regardless of supergranules) after being separated into bins analogously to Figure 3.6.

4.2.4 Imperfect kernel

The SOLA inversion method [14] utilizes vector averaging kernel – second order tensor $\boldsymbol{\mathcal{K}}^\alpha = (\mathcal{K}_x^\alpha, \mathcal{K}_y^\alpha, \mathcal{K}_z^\alpha)$. Specifically, final inverted velocity v can be expressed as:

$$v_\alpha\Big[(\boldsymbol{r}_0, z_o)\Big] = \int_\odot \boldsymbol{\mathcal{K}}^\alpha\Big[(\boldsymbol{r} - \boldsymbol{r}_0, z), z_o\Big] \cdot \boldsymbol{u}(x)\ \mathrm{d}^2\boldsymbol{r}\ \mathrm{d}z + N^\alpha \tag{4.1}$$

where $\odot$ denotes entire solar volume, $\boldsymbol{r}$ and $\boldsymbol{r}_0$ are horizontal position vectors, z and z_0 are heights, $\boldsymbol{u}$ is the actual velocity field and N denotes noise component.

Numerical values of $\boldsymbol{\mathcal{K}}$ are result of nontrivial optimizing procedure described in [14]. The values of the $\boldsymbol{\mathcal{K}}$ are visualized in Figure 4.10. Its north-south versus east-west asymmetry is likely the cause of the pattern with octagonal symmetry in Figure 4.4 and others like it.

4.3 Comparison with other observations

In [1] in Fig. 7 (b) there is a relation similar to our results, and (apart from sign convention) our results seem to agree with their results for the outflow regions.

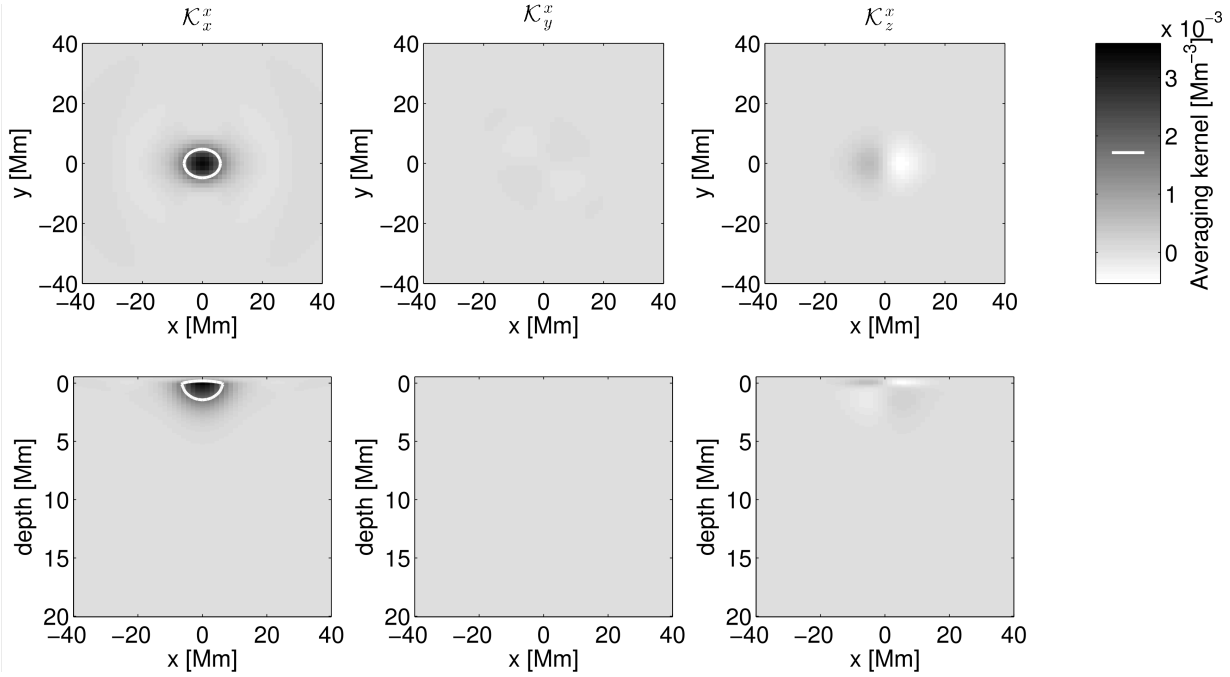

Figure 4.10: Visualization of averaging kernel – courtesy of M. Švanda.

4.4 Consistency with Coriolissian origins of vorticity

Coriolis force is a fictitious force acting on moving bodies within a rotating reference frame. The Sun however is subject to *differential* rotation, meaning there is no corotating frame of reference for the whole star. For a fixed latitude (and depth), rotation can be locally viewed as constant-rate rotation. we can therefore calculate coriolis parameters for every latitude φ:

$$f_r(\varphi) = 2 \sin \varphi \omega(\varphi) \tag{4.2}$$

where f_r is local coriolis parameter and ω is the angular velocity.

For a moving body the rotation rate is not even locally constant – there is a gradient. Since our data have been compensated for differential rotation, a testing body should behave as if an appropriate fictitious force [3] was acting upon the body. On the other hand, background flows [4] act against said fictitous force. Nonetheless, these forces affect vorticity in a nontrivial way, therefore we will calculate this "differential" parameter f_d:

$$f_d(\varphi) = \cos \varphi \frac{\mathrm{d}\omega(\varphi)}{\mathrm{d}\varphi}. \tag{4.3}$$

Both these parameters are shown in Figure 4.11 using ω from (1.2) and coefficient values from 1.3.

Figure 3.6 is qualitatively similar to f_r in Figure 4.11 in the relevant interval, especially when 4.2.2 is taken into account. We are unable to make a more

[3] corresponding with derivative of $\omega(\varphi)$

[4] associated with ω

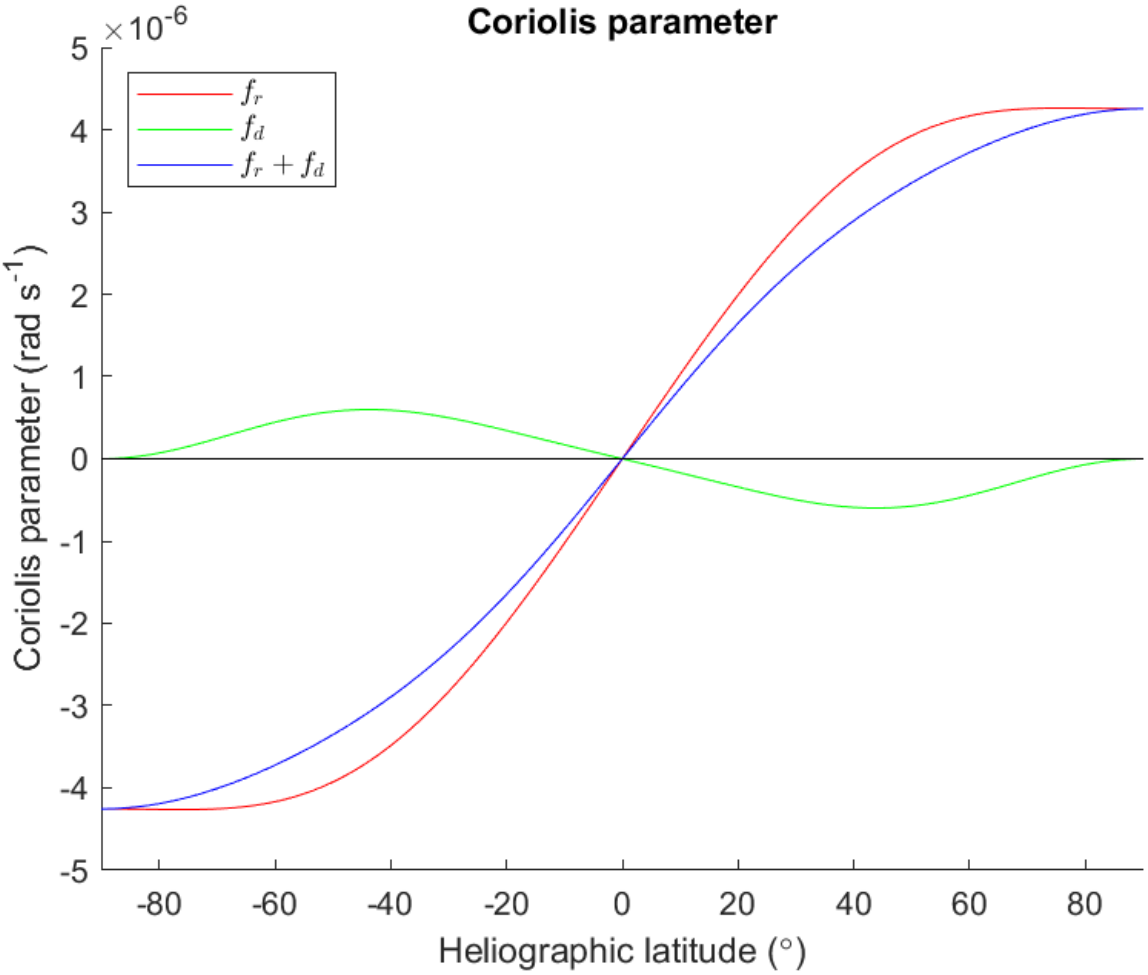

Figure 4.11: Dependence of coriolis parameter and circular velocity gradient (differential component) on heliographic latitude φ

quantitative comparison both because of the rather high uncertainty of our results (together with unimplemented further corrections) and a model of solar plasma mechanics is beyond the scope of this thesis. The nature of our results supports the hypothesis, however we cannot make any more conclusive statements.

Conclusion

We explored the nature of flows in the given dataset both in planes provided and around the average supergranule. Furthermore, we examined vortical motions near the centers of the supergranules and its relation to heliographic latitude of said center.

Since our resulting relation contains inconsistency – namely discontinuity between regions of measurement – without *definitive* explanation, we must conclude that our calculated datapoints have confidence intervals larger than calculated errorbars and possibly contain systematic biases, so the overall significance of our results is lowered.

We theorised several possible sources of inaccuracies that have not been fully examined. In case of further research, removing these unknowns would be the first step. If discontinuity remains, various elements in analysis should be replaced one by one and compare results; namely supergranule detection algorithm, vorticity calculation method, inversion method (or just numerical averaging kernel) and primary detectors.

Bibliography

[1] Langfellner, J.; Gizon, L. and Birch, A. C.: *Spatially resolved vertical vorticity in solar supergranulation using helioseismology and local correlation tracking.* AA 581, A67 (2015)

[2] Zirker, J. B.: *Sunquakes* Johns Hopkins University Press. p. 2.

[3] Bahng, J. and Schwarzschild, M.: *Lifetime of Solar Granules* The Astrophysical Journal. 134: 312.

[4] Christensen-Dalsgard, J.; Gough, D. O. and Thompson, M. J.: *The depth of the solar convection zone.* Astrophysical Journal, Part 1 (ISSN 0004-637X), vol. 378, Sept. 1, 1991, p. 413-437.

[5] Del Moro, D.;Berrilli, F.;Duvall, T. et al.: Dynamics and Structure of Supergranulation Solar Physics (2004) 221: 23.

[6] Emilio, M.; Kuhn, J. R.; Bush, R. I. and Scholl, I. F.: *Measuring the Solar Radius from Space during the 2003 and 2006 Mercury Transits.* The Astrophysical Journal 750 (2): 135

[7] Stix, M.: *The Sun : An Introduction.* 2nd Edition by Michael Stix. Astronomy and Astrophysics Library, Springer. ISBN: 3540207414

[8] Schwarzschild, K.; Voigt, H.: *Gesammelte Werke Collected Works.* vol. 1, 1992, Springer-Verlag Berlin Heidelberg, p 14

[9] Snodgrass, H. B. and Ulrich, R. K.: *Rotation of Doppler features in thr solar photoshpere.* The Astrophysical Journal, Part 1 (ISSN 0004-637X), vol. 351, March 1, 1990, p. 309-316.

[10] Kosovichev, A. G. et al.: *Structure and rotation of the solar interior: Initial results from MDI medium-l program.* Solar Physics (1997) 170: 43. (ISSN 0038-0938; 1573-093X)

[11] Duvall, T. L. Jr et al.: *Time-distance helioseismology.* Nature 362, 430–432 (1993)

[12] Scherrer, P. H. et al.: *The Helioseismic and Magnetic Imager (HMI) Investigation for the Solar Dynamics Observatory (SDO).* Solar Physics, Volume 275, Issue 1-2, pp. 207-227

[13] Schou, J. et al.: *Design and Ground Calibration of the Helioseismic and Magnetic Imager (HMI) Instrument on the Solar Dynamics Observatory (SDO).* Solar Physics, Volume 275, Issue 1-2, pp. 229-259

[14] Švanda, M.;Gizon, L.;Hanasoge, S. M. and Ustyugov, S. D.: *Validated helioseismic inversions for 3D vector flows.* The Astrophysical Journal, Volume 790, Issue 2, article id. 135, 7 pp. (2014)

[15] Švanda, M.;Sobotka, M.;Bárta, T.: *Moat flow system around sunspots in shallow subsurface layers*. The Astrophysical Journal, Volume 790 (2014), Issue 2, article id. 135,7 pp. (2014), section 3.2

[16] Snyder, J. P.: *Map projections: A working manual*. Professional Paper (1987) 1395: p. 191-202

[17] Rozelot, J.-P; Damiani, C.: *History of solar oblateness measurements and interpretation*. The European Physical Journal H 36(3):407-436

[18] Langfellner, J.; Birch, A. C. and Gizon, L.: *Evolution and wave-like properties of the average solar supergranule* AA 617, A97 (2018)

List of Figures

Attachments

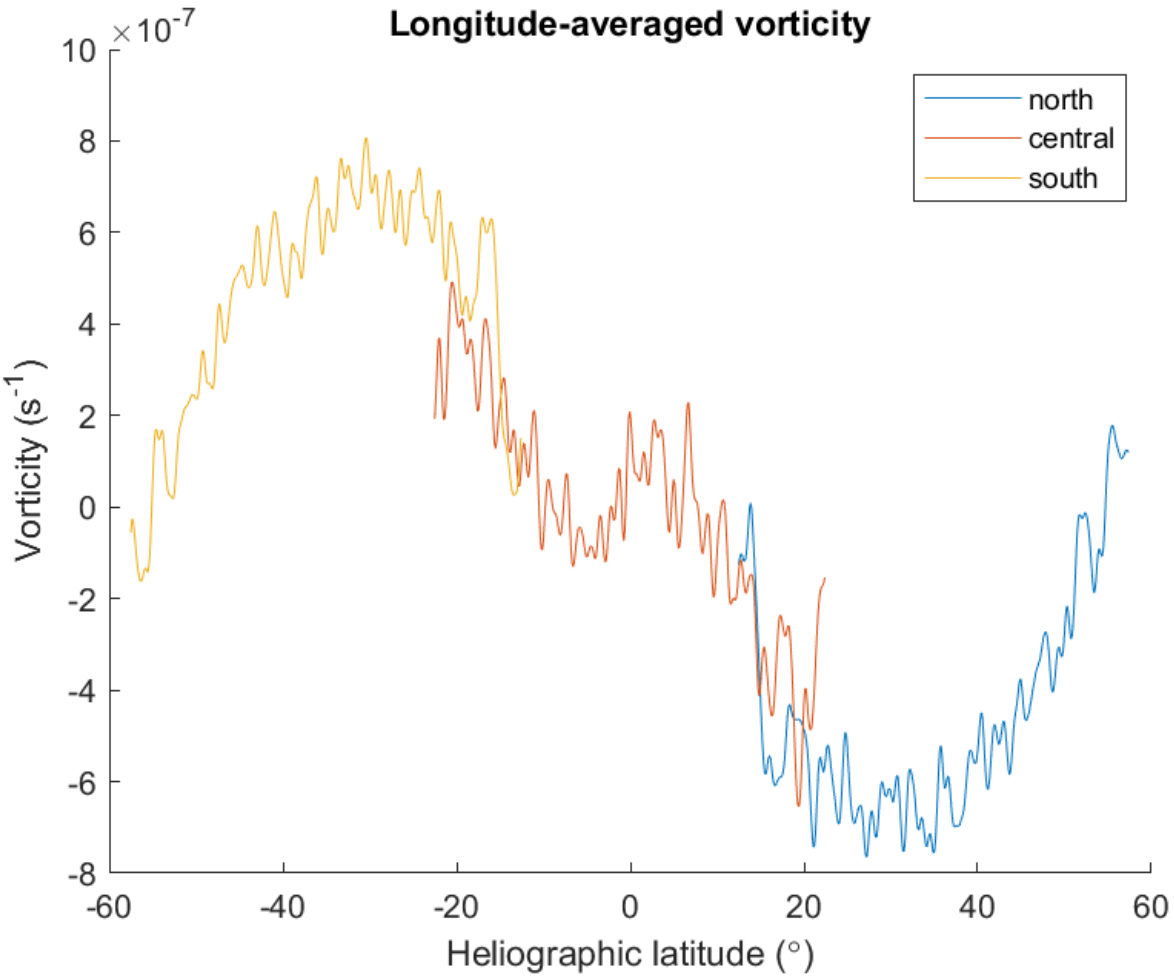

Figure 4.12: Average vorticity μ_d (regardless of supergranules) averaged along x-axis (Postelian longitude analogue).

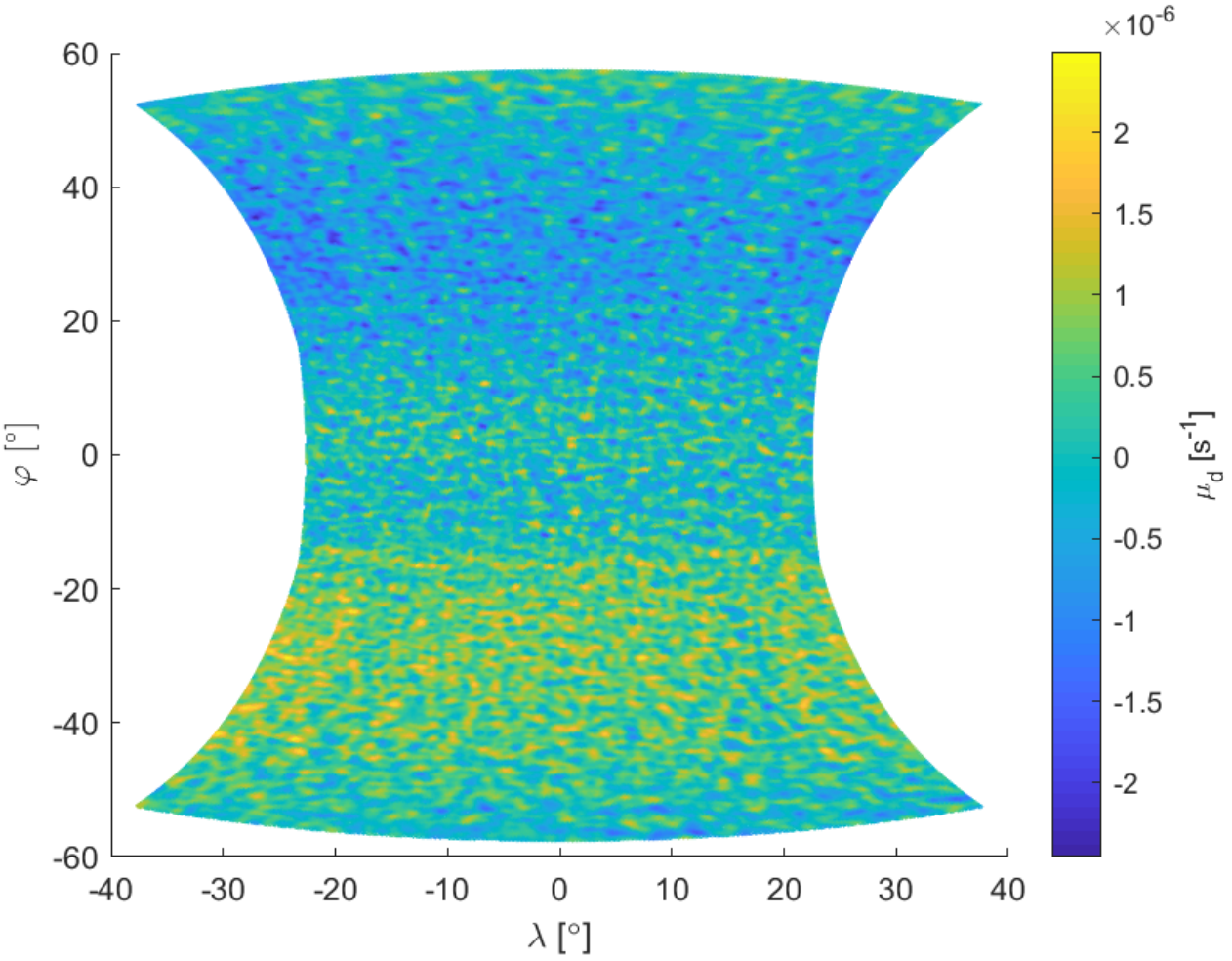

Figure 4.13: Average vorticity μ_d (regardless of supergranules) in heliographic coordinates – all regions.